Rare Metal Materials and Engineering
Volume 55, Issue 9, September 2026
Available online at www.rmme.ac.cn

Science Press

Cite this article as: Gao Chenguang, Pei Xuhui, Chen Zhuo, et al. Wide-Temperature-Range Tribological Properties of In Situ Ceramic-Reinforced TaMoTiCr Refractory High-Entropy Alloy Composites[J]. Rare Metal Materials and Engineering, 2026, 55(09): 2165-2178. DOI: https://doi.org/10.12442/j.issn.1002-185X.20240490.

ARTICLE

Wide-Temperature-Range Tribological Properties of In Situ Ceramic-Reinforced TaMoTiCr Refractory High-Entropy Alloy Composites

Gao Chenguang, Pei Xuhui, Chen Zhuo, Wang Hanming, Hu Mingchuan, Du Yin, Wang Haifeng

Center of Advanced Lubrication and Seal Materials, State Key Laboratory of Solidification Processing, Northwestern Polytechnical University, Xi'an 710072, China

Abstract: In-situ ceramic phase-reinforced TaMoTiCr refractory high-entropy alloy (RHEA) composites were prepared by spark plasma sintering with the addition of 2.5wt% and 5.0wt% h-BN, separately. Results show that the h-BN promotes the uniform formation of (Ti, Ta)N, TaB_2, and MoB ceramic phases within the body-centered cubic matrix, significantly increasing microhardness to 1136.95 HV. Tribological test results show that the composite with the addition of 2.5wt% h-BN presents great performance at room temperature with an ultra-low wear rate of 1.64×10^{-7} $mm^3\cdot N^{-1}\cdot m^{-1}$, while the composite with the addition of 5.0wt% h-BN shows optimal performance at 300 °C. Above 800 °C (elevated temperature condition), lubricious oxide tribolayers, rich in Cr_2O_3, TiO_2, and B_2O_3, form on the material surface, effectively reducing friction and wear. At 1000 °C, the composite with the addition of 2.5wt% h-BN achieves a wear rate of 5.22×10^{-7} $mm^3\cdot N^{-1}\cdot m^{-1}$. This in situ ceramic reinforcement approach effectively enhances wear resistance of RHEAs across a wide temperature range, offering great potential for advanced aerospace applications.

Key words: refractory high-entropy alloy ceramic composite; in-situ ceramic phase; tribological performance; spark plasma sintering

1 Introduction

With the rapid development of aerospace technology, metallic components in advanced systems face increasingly harsh tribological conditions. This tribological behavior significantly impacts the equipment reliability, stability, and lifespan[1]. Conventional superalloys experience a significant deterioration in strength and hardness under extreme high-temperature conditions, thereby leading to severe wear that jeopardizes the service reliability of high-temperature components[2–5]. Consequently, improving material tribological performance under varied conditions has become a key challenge, driving the urgent need for wear-resistant bulk alloys or coatings with excellent wide-temperature-range tribological properties. High-entropy alloys (HEAs) represent an innovative alloy design strategy, which contain four or more principal elements in equimolar or near-equimolar ratios[6–8]. This strategy differs from traditional alloy design, which typically relies on a single base element with minor solute additions, and it has drawn significant interest in materials science[9]. Severe lattice distortion and chemical complexity are intrinsic features of high-entropy systems, enabling enhanced strength, elasticity, and damage tolerance[10–11]. Refractory high-entropy alloys (RHEAs) are usually composed of high-melting-point elements, such as Ta, Mo, Zr, Nb, W, and Ti, exhibiting excellent high-temperature strength[12–15] and thermal stability[16–18]. These multifunctional properties make RHEAs ideal candidates for wear-resistant self-lubricating materials in extreme aerospace environments.

Received date: September 23, 2025
Foundation item: National Natural Science Foundation of China (52504425, 52474426); Fundamental Research Funds for the Central Universities (24GH0201107); Innovation Capability Support Plan in Shaanxi Province-Innovative Research Team for Science and Technology (2025RS-CXTD-019); Doctoral Dissertation Innovation Fund for Northwestern Polytechnical University (CX2024053)
Corresponding author: Du Yin, Ph. D., Center of Advanced Lubrication and Seal Materials, State Key Laboratory of Solidification Processing, Northwestern Polytechnical University, Xi'an 710072, P. R. China, E-mail: duyin@nwpu.edu.cn; Pei Xuhui, Ph. D., Center of Advanced Lubrication and Seal Materials, State Key Laboratory of Solidification Processing, Northwestern Polytechnical University, Xi'an 710072, P. R. China, E-mail: peixuhui@nwpu.edu.cn

However, the intrinsic brittleness and inferior oxidation resistance of RHEAs significantly restrict their practical applications. Most aerospace components operate under complex, fluctuating temperatures, requiring stable tribological properties and oxidation performance across a wide temperature range. For instance, RHEAs exhibit inferior plasticity at room temperature (RT), therefore hardly accommodating the friction-induced deformation, which leads to severe wear[19–21]. Compared with conventional wear-resistant alloys, such as TC4[22,24], Ti6Al4V[25], and SS304[26], RHEAs show much higher wear rates at RT, highlighting the urgent need to improve their wear resistance. Although compositional tuning can improve the plasticity and wear resistance of RHEAs, the extent of enhancement in their mechanical properties remains restricted[27–28]. Metal matrix composites incorporating ceramic phases offer enhanced strength and hardness, thus achieving superior wear resistance. For example, Gu et al[29] introduced SiC into $Fe_{50}Mn_{30}Co_{10}Cr_{10}$ alloy via arc-melting, attaining excellent strength-ductility synergy and a low wear rate of 2.89×10^{-6} $mm^3\cdot N^{-1}\cdot m^{-1}$. Deng et al[30] demonstrated that B_4C addition significantly improved strength and wear resistance with abrasive wear as the dominant mechanism at RT. Liu et al[31] used laser cladding to incorporate TiC into CoAlTiWTa coatings and reported that a 5wt% TiC addition led to high hardness and excellent wear performance. Ceramic-reinforced RHEA composites combine the high hardness of ceramics with multifunctional properties of RHEAs, greatly improving surface load capacity and wear resistance. However, current research is rare. Most studies rely on direct blending to introduce ceramics, which often causes interfacial incompatibility[32] or particle agglomeration[33], hindering further development. Thus, advanced processing strategies for bulk ceramic-reinforced RHEA composites are urgently needed.

Additionally, elevated temperatures induce severe oxidative corrosion on alloy surfaces, significantly degrading the tribological properties. RHEAs typically exhibit rough worn surfaces and have high coefficients of friction (COFs) during sliding due to their inferior oxidation resistance[34–35]. It is demonstrated that self-generated protective oxide layers (Cr_2O_3 and $CrTaO_4$) can effectively suppress oxygen diffusion, imparting RHEAs with superior oxidation resistance[36–37]. Consequently, Cr-containing RHEAs serve as preferred matrix materials for ceramic-reinforced RHEA composites. Meanwhile, researchers found that boronizing treatments on HEAs can enhance wear resistance and significantly reduce COFs[38–39]. The resultant borides not only function as reinforcing phases but also form boron-containing tribolayers with favorable lubricating properties. Boron oxide (B_2O_3), a distinctive lubricative oxide, melts at high temperatures to form quasi-liquid adaptive lubricating films to provide stable lubrication through viscous flow mechanisms[40]. Therefore, incorporating boride ceramic phases can enhance the tribological performance of composites.

As an advanced powder metallurgy technique, spark plasma sintering (SPS) is widely used to produce ceramics, nanomaterials, and particle-reinforced metal matrix composites[38]. By applying uniaxial pressure and pulsed electrical current, SPS enables fast densification at lower temperatures, suppresses grain growth, and achieves microstructure control. It also reduces porosity and yields components with excellent mechanical properties[23], making it optimal for fabricating ceramic-reinforced RHEA composites. During high-temperature SPS, in-situ chemical reactions can generate ceramic precipitates within the alloy matrix[45], which exhibit stronger interfacial bonding and better thermodynamic stability than directly added ceramic phases[23]. Thus, using in-situ reactions in SPS to fabricate ceramic-reinforced RHEA composites is a highly promising approach.

This study employed SPS to fabricate TaMoTiCr matrix composites reinforced with multiple ceramic phases. The addition of h-BN facilitated the in-situ synthesis of (Ti, Ta)N, TaB_2, and MoB ceramic phases. By analyzing the microstructure and phase composition of the composites, their microstructural evolution mechanism was revealed. Furthermore, the wear tests were conducted to investigate their wear resistance mechanism at RT and their lubrication mechanism at ultra-high temperatures. This work provided theoretical guidance for studying the tribological properties of in-situ reacted ceramic-reinforced RHEA matrix composites. The design of ceramic-reinforced RHEA composites provided new insights for optimizing high-performance solid lubricants in engineering applications.

2 Experiment

RHEA-based solid lubricant composites $TaMoTiCr(BN)_x$ with x=2.5 and 5.0 (wt%), denoted as BN2.5 and BN5, respectively, were fabricated using high-energy ball milling followed by SPS. High-purity powders of Ta (about 48 μm), Mo (about 48 μm), Ti (about 48 μm), Cr (about 48 μm), and h-BN (about 48 μm) served as raw materials. The high-energy ball milling process was conducted using a planetary ball mill (YXQM-4L, Miqi China) under an argon atmosphere. An equiatomic mixture of Ta, Mo, Ti, and Cr powders (total mass of 50 g) was prepared within an inert atmosphere and milled with WC balls at a ball-to-powder ratio of 10∶1 and a milling speed of 350 r/min for 20 h. Subsequently, 2.5wt% and 5.0wt% h-BN powders were added to the pre-milled RHEA powder, separately, followed by milling for 2 h. For consolidation, the $TaMoTiCr(BN)_x$ powder mixtures were loaded into a graphite die with an inner diameter of 30 mm. The powders were pre-compacted at RT under 50 MPa for 10 min and then sintered using SPS system (HP D25, FCT Systeme GmbH, Germany). SPS process involved heating to 1800 °C at a heating rate of 100 °C/min, holding at the designed temperature under 50 MPa for 10 min, and final water quenching to RT to obtain bulk composites. The as-sintered cylindrical samples were sectioned using wire electrical discharge machining. Then, the surfaces were ground stepwise using SiC abrasive paper from 400# to 2000# and mechanically polished to a mirror finish using a SiO_2

suspension for subsequent characterization.

The microstructures of BN2.5 and BN5 composites were investigated using X-ray diffractometer (XRD; D8, Bruker, Co-Kα radiation), scanning electron microscope (SEM; Helios G4 CX, FEI), and energy-dispersive X-ray spectroscope (EDS; X-MaxN, Oxford Instruments). Dry reciprocating sliding wear tests were performed at RT, 300, 600, 800, and 1000 ° C employing a high-temperature ball-on-disk tribometer (LMT-5000, Rtec). An Al_2O_3 ball (diameter of 9.525 mm) was used as the counterpart under the following constant conditions: normal load of 10 N, stroke length of 1 mm, reciprocating frequency of 5 Hz, and test duration of 30 min. The tests were repeated at least three times under each condition to ensure data accuracy. The wear volume of all samples was measured using white light interferometric profilometry (Contour GT-K, Bruker). The wear tracks on the composites and the worn surfaces of the corresponding Al_2O_3 balls were analyzed for morphology and composition using SEM and EDS. X-ray photoelectron spectroscope (XPS; PHI 5000 VersaProbe III, ULVAC-PHI) was employed to detect the chemical states of the wear tracks under various test conditions and to analyze the types of oxidized products generated after friction and wear testing.

3 Results and Discussion

3.1 Microstructure characterization

Fig. 1 presents XRD patterns of BN2.5 and BN5 ceramic-reinforced RHEA composites. Both samples exhibit a single-phase body-centered cubic (bcc) RHEA matrix with lattice parameters of 0.3143 (BN2.5) and 0.3118 (BN5) nm. The slight lattice expansion is attributed to the consumption of molybdenum (atomic radius: 0.134 nm), the smallest atom in bcc phase, during ceramic phase formation[41]. In both composites, in-situ formed ceramic phases include (Ti, Ta)N (JCPDS# 99-2759, 99-3636), TaB_2 (JCPDS# 38-1462), and MoB (JCPDS# 06-0644). Notably, no peaks corresponding to h-BN are observed in both composites, indicating complete reaction consumption of the added h-BN during SPS without residual phases. h-BN is introduced into the TaMoTiCr RHEA system as a combined boron and nitrogen source to promote in-situ formation of ceramic phases. As a high-potential inorganic material, h-BN offers ultra-low friction, excellent thermal stability (decomposition>2500 °C in inert atmospheres[42]), and the ability to dissolve in metals and participate in redox reactions to form hard ceramics[43]. Structurally, h-BN resembles graphene, featuring a layered honeycomb arrangement of alternating B and N atoms. In this research, SPS was conducted at a peak temperature of 1800 °C under 50 MPa in an argon atmosphere. The complete disappearance of h-BN in XRD analysis confirms its full consumption via redox reactions with refractory elements.

Entropy-driven order-to-disorder transitions can significantly affect phase stability and defect evolution in multi-principal element systems, which can influence the formation and structural stability of in-situ ceramic phases during SPS process[47]. These reactions illustrate the mechanisms underlying in-situ ceramic phase formation, as follows:

$$3Ti + 2BN \rightarrow 2TiN + TiB_2 \quad (1)$$

$$Ta + 2BN \rightarrow 2TaN + TaB_2 \quad (2)$$

The ceramic phases in the composite material are formed through redox reactions between the matrix and h-BN. To gain deeper insight into the competitive reaction mechanisms governing the formation of boride and nitride phases, FactSage software was used to calculate the variation in Gibbs free energy for different ceramic phases as a function of temperature, as shown in Fig. 2. The results indicate that within the temperature range of 100–2200 °C, the Gibbs free energy of TiN is significantly lower than that of TiB_2 and other nitrides, such as Ta_2N, TaN, and MoN. Consequently, Ti tends to preferentially react with N to form the TiN ceramic phase. This preference is further supported by the notably lower Gibbs free energy of TiN at 1800 °C (−483.64 kJ·mol^{-1}) compared with that of TiB_2 (−239.68 kJ·mol^{-1}), suggesting that Ti is expected to react with N prior to other elements during SPS. The remaining N subsequently reacts with Ta to form TaN phases. In contrast, Mo and Cr exhibit relatively inferior affinity for N, placing them at a disadvantage in the competitive reactions. Among the boride ceramic phases, TiB_2 possesses the lowest Gibbs free energy. However, since Ti is largely consumed by prior reactions with N, the remaining B preferentially reacts with Ta to form TaB_2, while a small amount of B also reacts with Mo to produce MoB. The

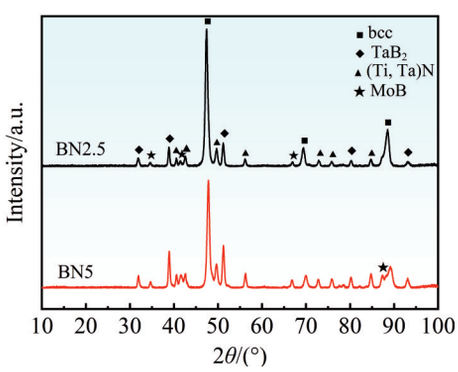

Fig.1 XRD patterns of BN2.5 and BN5 ceramic-reinforced RHEA composites

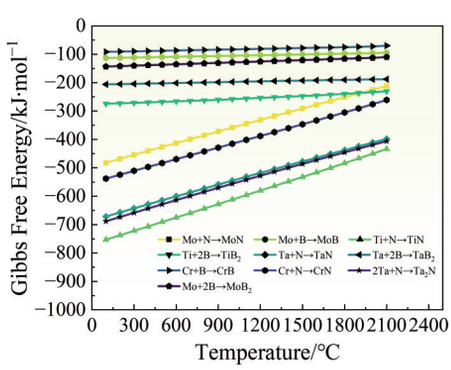

Fig.2 Calculated Gibbs free energy of ceramic phases at different temperatures by software FactSage

predicted reaction sequence is consistent with the phase identification results obtained from XRD.

Fig. 3 presents SEM images in secondary electron (SE) mode and EDS elemental mapping results of BN2.5 and BN5 ceramic-reinforced RHEA composites. Both samples exhibit typical multiphase microstructures with clear elemental segregation and distinct phase contrast. The matrix primarily consists of a light-gray bcc solid solution, which is identified as the TaMoTiCr RHEA phase. Finely dispersed dark-gray precipitates are attributed to TiN, while bright white regions correspond to in-situ formed ceramic phases, including TaB_2 and MoB, which is consistent with XRD results. EDS point scan data further elucidate the chemical composition of the phases, as listed in Table 1. It can be observed that the main metallic element in the precipitated phase is Ti, while N is significantly enriched in the precipitated phase with its content being much higher than that in other phases. Additionally, bright-white boride regions contain B of high content (about 65at%) with Ta (18at%–20at%) and Mo (5at%–7at%). These results suggest that Ta consumes partial available B to form TaB_2, while the remaining B reacts with Mo to generate MoB, leading to a mixed TaB_2 and MoB phase field. EDS elemental maps confirm the spatial distribution of key elements, validating the presence and uniform dispersion of the ceramic phases throughout the matrix. Notably, both composites exhibit high relative density and minimal porosity, indicating effective densification achieved through SPS at 1800 °C under 50 MPa. The actual densities of SPS materials were determined by Archimedes' method: 8.85 g/cm^3 for BN2.5 composite and 8.17 g/cm^3 for BN5 composite. The porosity is 3.99% and 3.10% for BN2.5 and BN5 composites, respectively. The low porosity levels attest to the effectiveness of SPS in producing dense composite materials. High-energy ball milling produces alloy powders with a homogeneous microstructure and composition, which facilitates efficient densification via SPS to yield composites with excellent hardness and wear resistance[48].

Atom-scale analysis reveals unique local chemical ordering and structural homogeneity in RHEAs, which provides a favorable foundation for fabricating composites via SPS, and

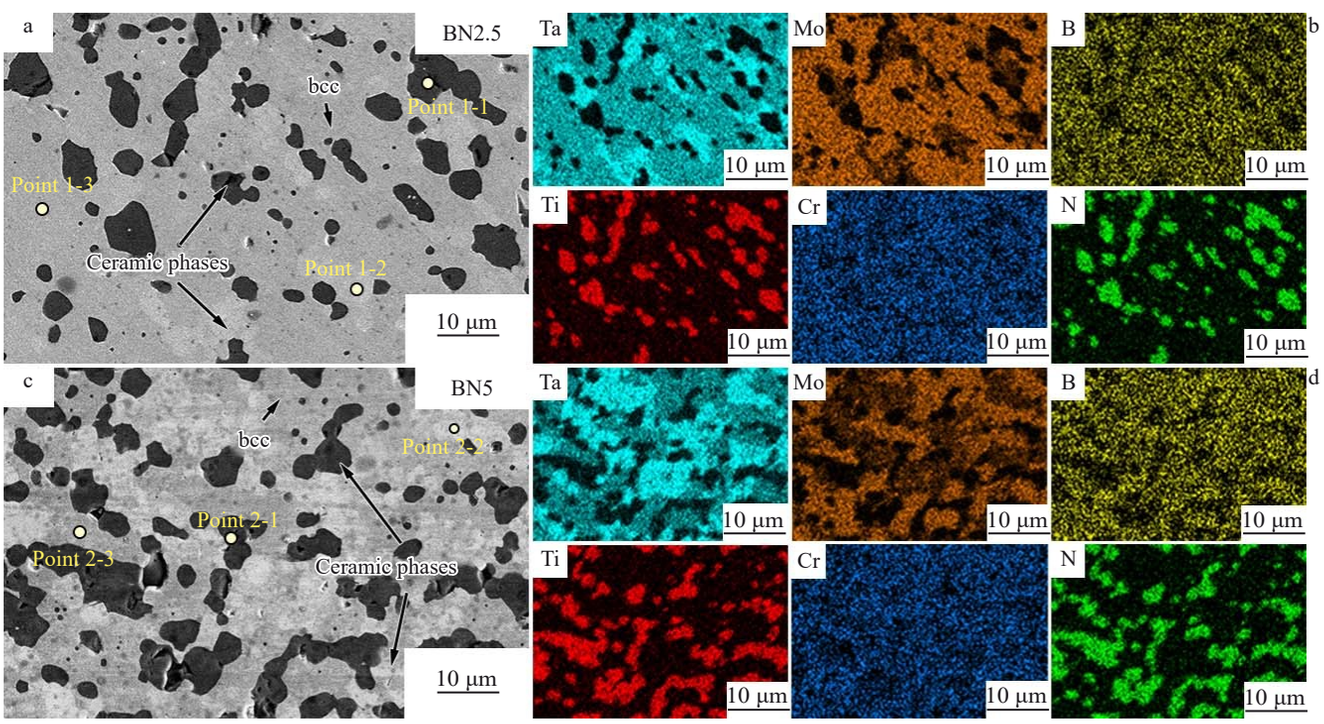

Fig.3 SEM-SE images (a, c) and EDS elemental mappings (b, d) of BN2.5 (a–b) and BN5 (c–d) ceramic-reinforced RHEA composites

Table 1 EDS results of points marked in Fig.3 (at%)

Point	Ta	Mo	Ti	Cr	B	N
1-1	0.75	0.02	48.1	0.18	20.71	30.24
1-2	19.98	6.50	2.29	5.68	65.55	0.00
1-3	16.19	20.05	4.77	17.06	41.93	0.00
2-1	0.49	0.04	47.73	0.16	20.63	30.95
2-2	17.68	4.73	2.62	5.80	69.17	0.00
2-3	16.89	20.93	5.03	17.6	39.55	0.00

the resultant composite possesses a uniform microstructure with uniformly dispersed ceramic phases[49]. Quantitative image analysis through ImageJ software reveals that the volume fraction of ceramic phase is increased with the increase in h-BN content: 34.35vol% ±1.66vol% for BN2.5 composite (Fig. 3a) and 57.175vol% ± 2.72vol% for BN5 composite (Fig.3c). This trend confirms that increasing h-BN addition promotes more extensive in situ reactions, leading to higher ceramic phase content within the composite microstructure. Importantly, the ceramic phases remain well-dispersed without visible agglomeration, suggesting favorable interfacial compatibility and stable phase formation during sintering.

3.2 Microhardness and tribological properties

According to Archard's empirical equation, higher hardness generally improves wear resistance[44]. Fig. 4 shows the microhardness of BN2.5 and BN5 composites is 1036.78±62.42 and 1136.95±116.87 $HV_{1.0}$, respectively. The higher microhardness of BN5 composite results from increased ceramic phase content due to more h-BN addition. Hard nitrides and borides, such as TaN (>4080 HV[50]), TiN (2510 HV[46]), TiB_2 (3060 HV[51]), and MoB (> 2000 HV[52]) exist in the composites. These ceramic phases significantly improve the composite hardness by reinforcing the matrix[53] and hindering dislocation motion[54].

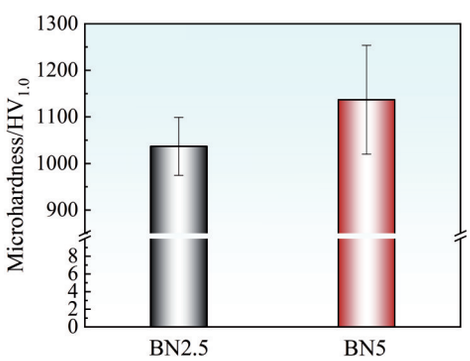

Fig.4 Microhardness of BN2.5 and BN5 ceramic-reinforced RHEA composites

Wear test results for BN2.5 and BN5 composites are shown in Fig.5–Fig.6. All samples display a clear running-in stage at the beginning of sliding (Fig.5a–5e), characterized by a rapid increase in COF due to surface damage, debris accumulation, and oxide formation[55]. The duration of this stage depends on several factors, such as hardness, surface roughness, and temperature. As oxidation and thermal softening progress, COF becomes lower, eventually leading to a dynamic balance (a steady wear stage with stabilized COF). Throughout the wear tests, the BN5 composite consistently shows lower COF values than BN2.5 composite at all temperatures (Fig.5a–5e), and its average steady-state COF is significantly reduced (Fig. 5f). Notably, at 800 °C, the BN5 composite exhibits a COF value of 0.30, which is much lower than that of BN2.5 composite (0.47). This result demonstrates that increasing h-BN content enhances hardness while effectively reducing friction. Both composites follow a similar trend with the increase in temperature: for BN2.5 composite, COF initially increases, reaches a peak value at 300 °C, and then decreases; for BN5 composite, COF rises from 0.38 (RT) to 0.48 (300 °C), then drops to 0.46 (600 °C), 0.30 (800 °C), and finally decreases to 0.24 (1000 °C). The reduction in COF beyond 300 °C may be attributed to the formation of lubricious oxide layers at

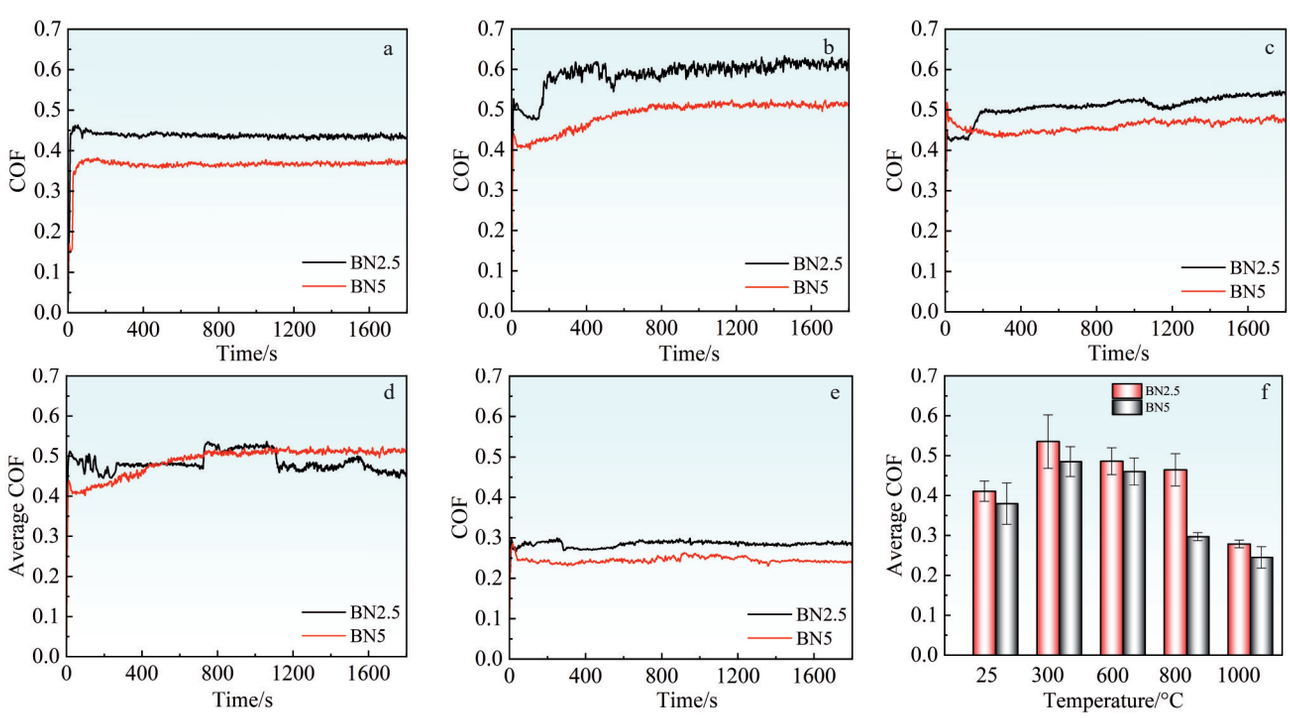

Fig.5 COF curves (a–e) and average COF values (f) of BN2.5 and BN5 ceramic-reinforced RHEA composites at different temperatures: (a) RT, (b) 300 °C, (c) 600 °C, (d) 800 °C, and (e) 1000 °C

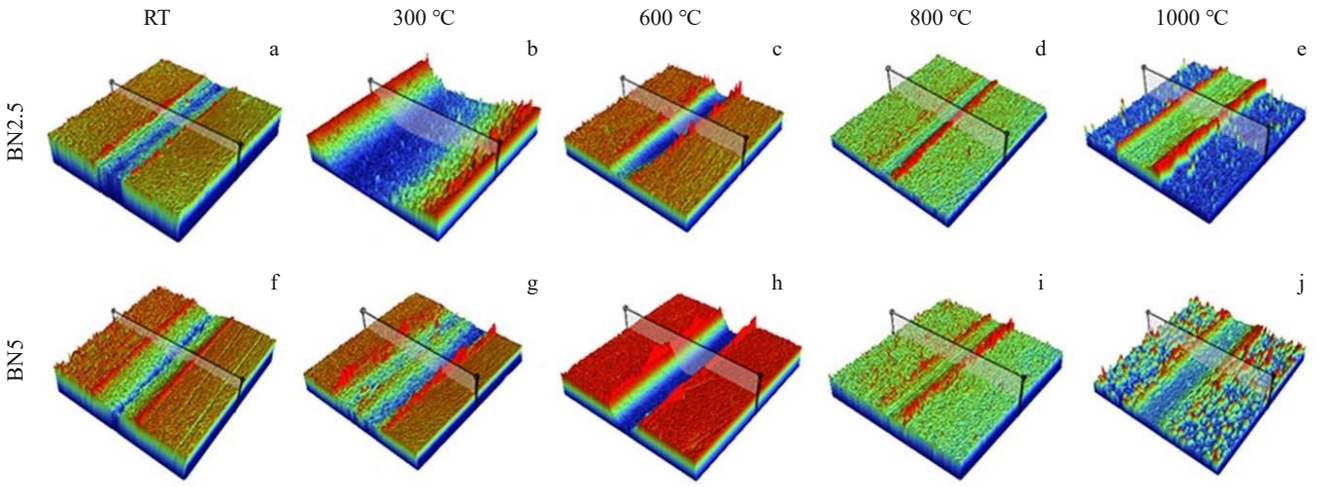

Fig.6 3D optical profiles of worn surfaces of BN2.5 (a – e) and BN5 (f – j) ceramic-reinforced RHEA composites at different temperatures: (a, f) RT, (b, g) 300 °C, (c, h) 600 °C, (d, i) 800 °C, and (e, j) 1000 °C

elevated temperatures.

Fig. 6 presents 3D surface topographies of wear tracks of BN2.5 and BN5 composites. Fig. 7 shows cross-sectional wear tracks and wear rates of BN2.5 and BN5 composites. Fig. 8 shows SEM-SE images of worn surfaces and corresponding EDS element mappings of BN2.5 and BN5 composites at different temperatures.

It can be seen that BN2.5 composite exhibits the shallowest wear depth and narrowest wear width, corresponding to its lowest wear rate at RT. At 300 °C, the BN5 composite demonstrates significantly smaller wear depth and width than BN2.5 composite. Besides, BN5 composite shows markedly shallower and narrower wear track at 300 °C, which is consistent with its minimal wear rate. Conversely, at 600 °C, increasing h-BN addition enlarges both wear depth and wear width, accompanied by elevated wear rates. Deepening wear tracks can be observed. Additionally, the material pile-up occurs along both sides of wear tracks for BN2.5 and BN5 composites at 800 and 1000 °C. This result manifests as tracks protruding above the material surface. This phenomenon occurs because wear debris generated during friction is driven by shear stresses to migrate along the sliding direction toward the wear track edges, leading to progressive accumulation. As high-temperature friction continues, the debris undergoes repeated compaction and volumetric expansion, ultimately causing the wear track to protrude above the base material[56].

Comparative analysis of wear rates in Fig. 7f reveals that BN2.5 composite reaches its maximum wear rate at 300 °C, and subsequently, it is decreased with the increase in temperature. In contrast, the wear rate of BN5 composite peaks at 600 °C,

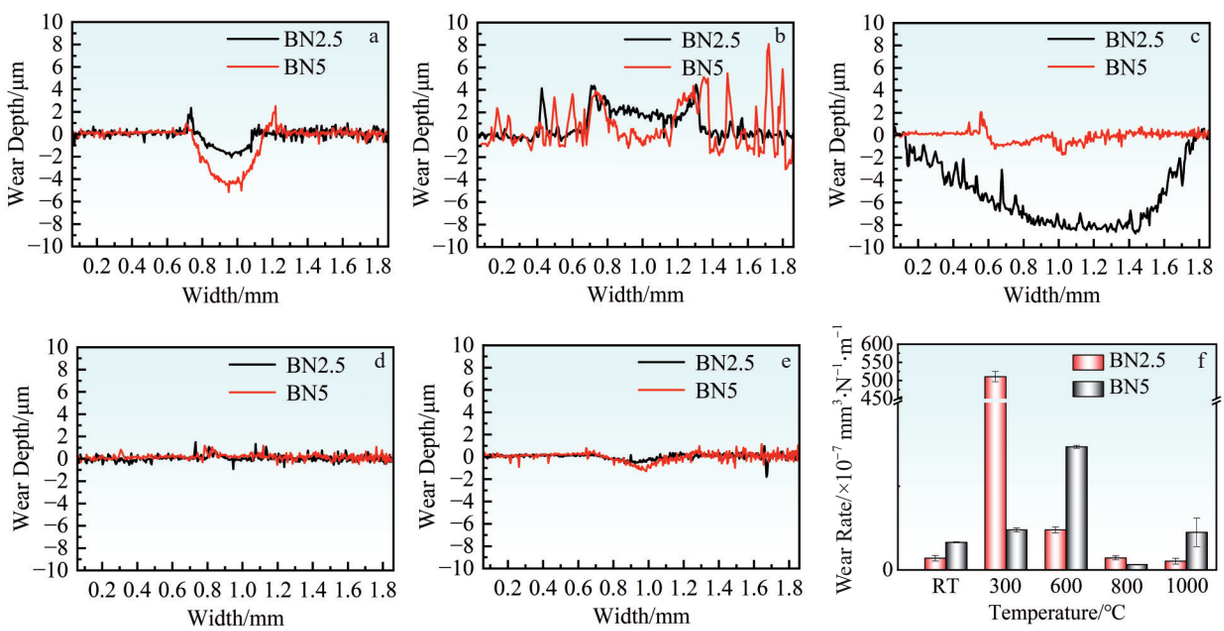

Fig.7 Cross-section profiles of wear tracks (a – e) and wear rates (f) of BN2.5 and BN5 ceramic-reinforced RHEA composites at different temperatures: (a) RT, (b) 300 °C, (c) 600 °C, (d) 800 °C, and (e) 1000 °C

and then decreases when temperature elevates from 800 °C to 1000 °C. Thus, BN2.5 composite achieves the lowest wear rate at RT $(1.64\pm0.02)\times10^{-7}$ $mm^3\cdot N^{-1}\cdot m^{-1}$, while BN5 composite has a wear rate of $(1.65\pm0.03)\times10^{-6}$ $mm^3\cdot N^{-1}\cdot m^{-1}$. At 300 °C, BN5 composite demonstrates superior wear resistance with a wear rate of $(2.39\pm0.11)\times10^{-6}$ $mm^3\cdot N^{-1}\cdot m^{-1}$, and the wear rate of BN2.5 composite is $(1.89\pm0.19)\times10^{-5}$ $mm^3\cdot N^{-1}\cdot m^{-1}$. Microstructure analysis of $TaMoTiCr(BN)_x$ composites suggests that reduced wear rates at RT and 300 °C may correlate with hard ceramic phases. These phases enhance matrix hardness and deformation resistance, thereby improving wear resistance. Above 600 °C, the wear rate of BN2.5 composite declines from $(2.39\pm0.12)\times10^{-6}$ $mm^3\cdot N^{-1}\cdot m^{-1}$ to $(5.22\pm0.17)\times10^{-7}$ $mm^3\cdot N^{-1}\cdot m^{-1}$ (1000 °C). Conversely, BN5 composite exhibits irregular trends. Its wear rate is $(3.23\pm0.2)\times10^{-7}$ $mm^3\cdot N^{-1}\cdot m^{-1}$ at 800 °C, which is lower than that of BN2.5 composite. However, at both 600 and 1000 °C, the wear rates of BN5 composite are $(7.36\pm0.09)\times10^{-6}$ and $(2.25\pm0.85)\times10^{-6}$ $mm^3\cdot N^{-1}\cdot m^{-1}$, respectively, which are higher than those of BN2.5 composite. The degraded wear resistance of BN5 composites at 600 and 1000 °C may be related to the high-temperature chemical transformations. Ceramic phases potentially compromise oxide film integrity on worn surfaces, adversely affecting friction performance.

3.3 Wear and lubricant mechanism

To understand the wear mechanisms of BN2.5 and BN5 composites at different temperatures and to evaluate the influence of ceramic phases on the tribological behavior of TaMoTiCr RHEAs, the worn surface morphologies after sliding tests were analyzed, as shown in Fig. 8. At RT, both composites show localized tribolayers and shallow ploughing grooves (Fig. 8a and 8e), indicating dominant abrasive wear. The BN2.5 composite exhibits continuous tribolayers with parallel grooves along the sliding direction, whereas the BN5 composite shows cracks, delamination, spalling pits, and exposed ceramic phases, but fewer visible grooves. As confirmed in Fig. 3 and Fig. 4, dispersed hard phases, such as TiN and TaB_2, enhance the surface hardness of BN5 composite, improving the resistance against the Al_2O_3 counterface ploughing[54]. However, the higher ceramic content in BN5 composite also induces embrittlement, promoting crack formation and brittle fracture, which accelerates wear. Thus, the wear rate of BN5 composite is higher at RT[55].

At 300 °C, reduced ploughing grooves exist on worn surfaces of both composites with localized tribolayers in partial areas. However, these tribolayers diminish significantly compared with those at RT. Comparative analysis reveals the distinct wear mechanisms: for the BN2.5 composite, sparse tribolayers, abundant wear debris, and severe delamination exist, indicating dominant adhesive wear (Fig. 8b); for the BN5 composite, fewer debris, delamination, micropits, but more extensive tribolayers can be observed, inferring the abrasive wear (Fig. 8f). The ceramic phase content plays a crucial role in determining the wear mechanism: lower content in BN2.5 composite results in reduced hardness and promotes adhesive wear, whereas higher content in BN5 composite enhances hardness, shifting the dominant mechanism toward abrasive wear. At 300 °C, elevated temperatures enhance atomic diffusion at the contact interface, promoting the formation of adhesive junctions. In the absence of protective oxide layers, fresh metal surfaces are exposed, causing the transition from abrasive wear to adhesive wear in BN2.5 composite. In contrast, the presence of hard ceramic phases in BN5 composite alters the wear mechanism, maintaining the primary abrasive wear at this temperature. Adhesive wear results from cold welding and interfacial shear, producing large debris, while the abrasive wear involves micro-cutting by the counterface[19]. In BN5 composite, the shift to abrasive wear reduces material transfer and surface damage, which explains its much lower wear rate at 300 °C. During dry sliding at 600 °C, BN2.5 composite develops complete tribolayers without significant scratches or debris (Fig. 8c). During sliding, wear debris and oxide particles can agglomerate through tribological interactions, gradually resulting in hard, smooth surface films through sintering and compacting, and the films are identified as glaze layers[56]. These layers act as a barrier between the metal and counterface, reducing interfacial shear and significantly lowering wear rates[57]. Driven by oxide formation, the high-temperature wear process in the composites is controlled by structural disorder and the concomitant evolution of defects, which dictate the energy dissipation[61]. EDS analysis of BN5 composite (Fig. 8h) reveals the absence of a continuous oxide tribolayer at this temperature, while concurrent thermal softening contributes to an increased wear rate. At 800 and 1000 °C, both composites develop continuous tribolayers. EDS analysis confirms that these layers are composed of dense oxides, indicating oxidative wear as the dominant mechanism at high temperatures. Notably, the tribolayer of BN2.5 composite has more pores than that of BN5 composite, which contributes to the overall reduction in wear rates at elevated temperatures. Crucially, BN-modified surfaces exhibit numerous micropits and cracks at 600 °C. After the tests at 800 °C, deep ploughing grooves can be observed in both composites. This damage arises likely from the mismatches in the thermal expansion coefficients (CTEs) between the ceramic phases and the TaMoTiCr matrix. Such CTE differences at elevated temperatures induce internal thermal stresses that weaken phase interfaces, promoting crack initiation and spalling, thereby degrading the wear performance[58–59]. SEM observations of cracks and micropits support this mechanism. Furthermore, differences in oxidation behavior between the ceramic phases and RHEA matrix may disrupt protective oxide layers, accelerating the oxidative corrosion of the matrix and reducing the high-temperature wear resistance[60].

To further explore the wear mechanisms, SEM and EDS analyses were conducted on Al_2O_3 counterfaces after wear tests with BN2.5 and BN5 composites at various temperatures, as shown in Fig. 9 and Fig. 10, respectively. Large wear scars can be observed on the counterfaces of

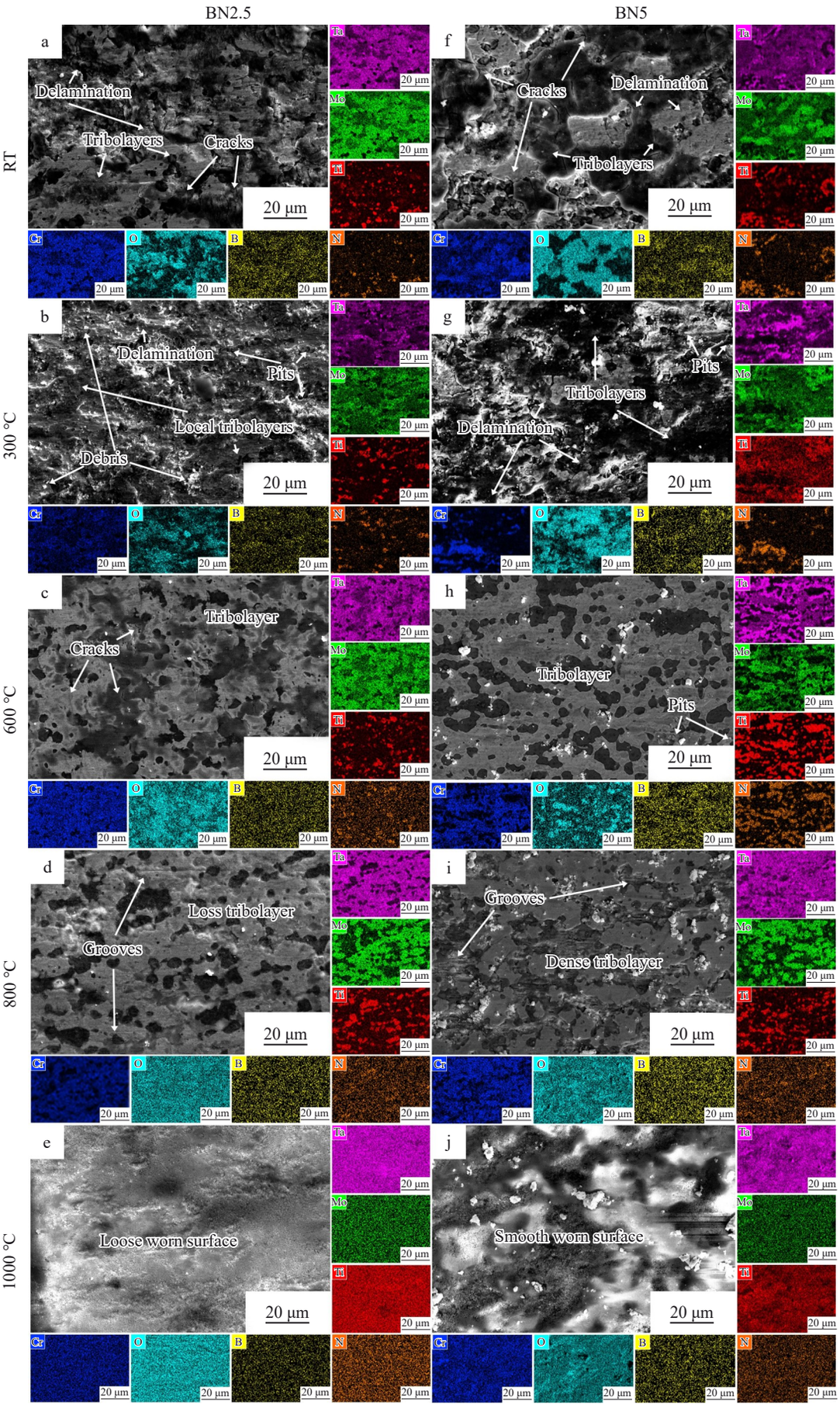

Fig.8 SEM-SE images of wear tracks for BN2.5 and BN5 ceramic-reinforced RHEA composites after sliding wear tests at different temperatures

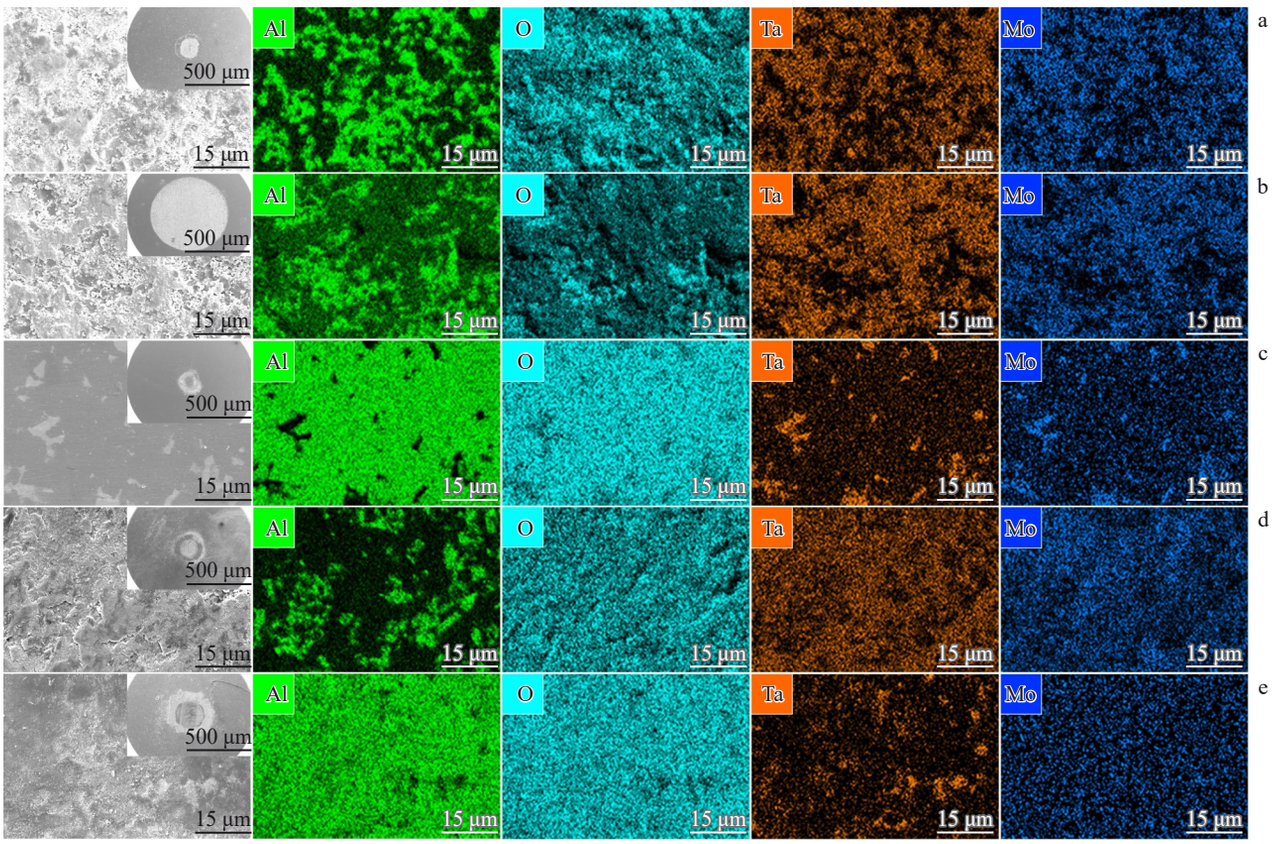

Fig.9 Worn surface morphologies and corresponding EDS element mappings of Al_2O_3 balls corresponding to BN2.5 composite at different temperatures: (a) RT, (b) 300 °C, (c) 600 °C, (d) 800 °C, and (e) 1000 °C

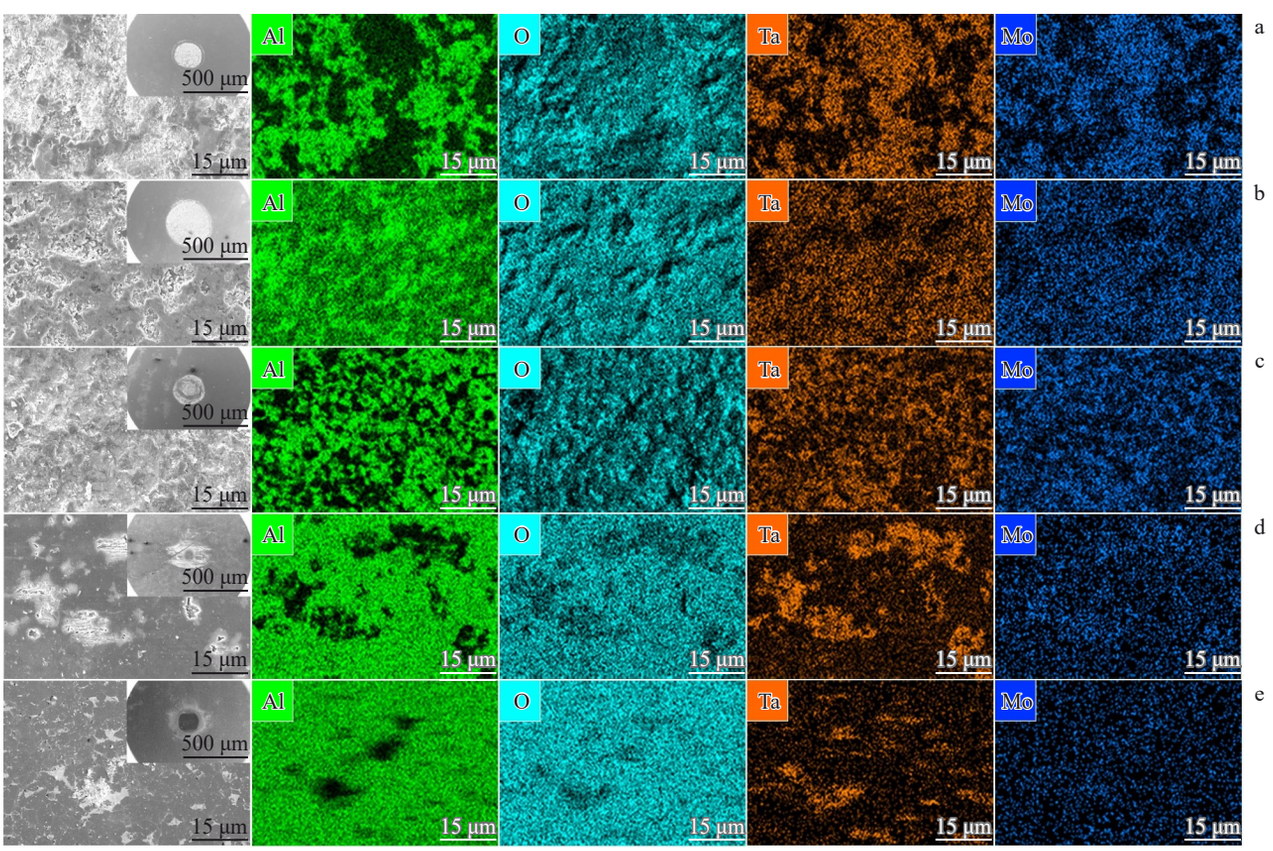

Fig.10 Worn surface morphologies and corresponding EDS element mappings of Al_2O_3 balls corresponding to BN5 composite at different temperatures: (a) RT, (b) 300 °C, (c) 600 °C, (d) 800 °C, and (e) 1000 °C

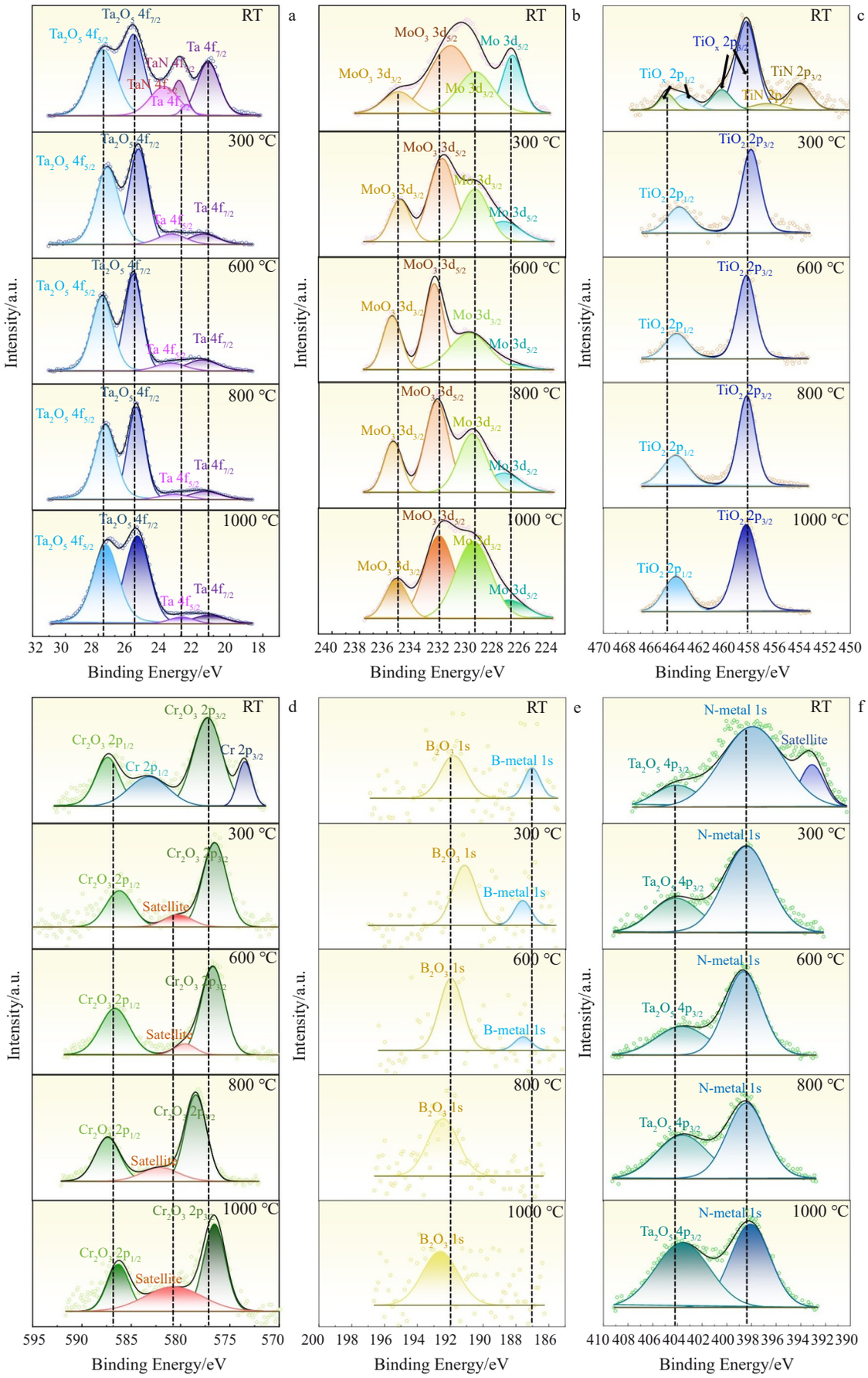

Fig.11 High-resolution XPS spectra of worn surfaces of BN2.5 composite at different temperatures: (a) Ta 4f, (b) Mo 3d, (c) Ti 2p, (d) Cr 2p, (e) B 1s, and (f) N 1s

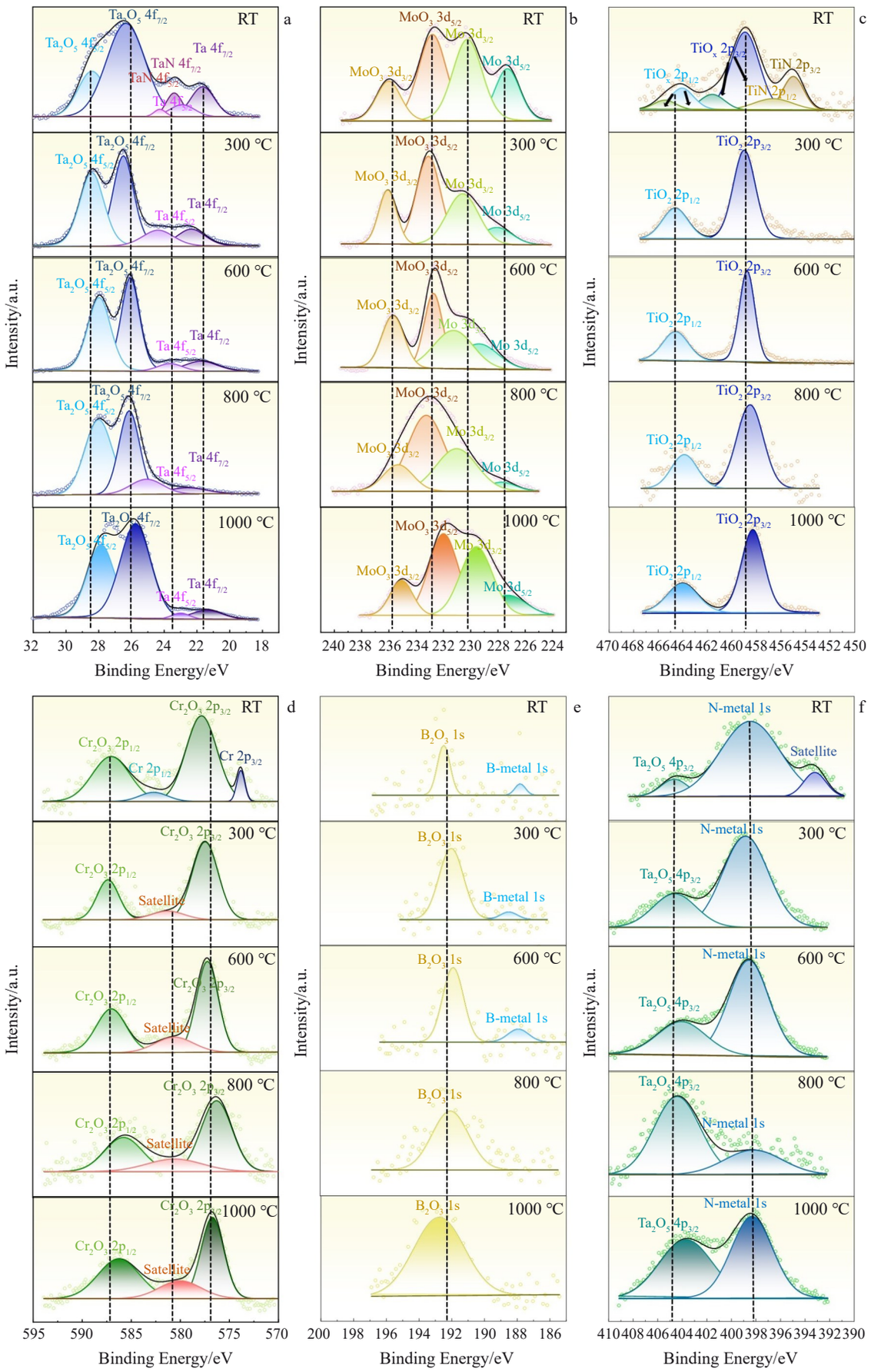

Fig.12 High-resolution XPS spectra of worn surfaces of BN5 composite at different temperatures: (a) Ta 4f, (b) Mo 3d, (c) Ti 2p, (d) Cr 2p, (e) B 1s, and (f) N 1s

BN2.5 composites than BN2.5 composites at RT, and the material transfer from BN5 composite is more severe, which is consistent with relatively higher wear rate of BN5 composite at RT. At 300 °C, the BN5 composite exhibits smaller counterface scars with significantly less material transfer than the BN2.5 composite. Above 600 ℃, dense oxide layers impede the direct alloy-counterface contact. Reduced adhesion zones can be observed in BN2.5 composite at 600 °C and in BN5 composite at 800 ℃, suggesting that the material transfer only occurs along scar edges. In contrast, the BN5 composite suffers severe transfer at 600 ℃ aligning with its higher wear rate. At 1000 ℃, material transfer nearly disappears, and both composites show small smooth contact areas on Al_2O_3 balls, demonstrating effective friction reduction by high-temperature oxide tribolayers. The BN5 composite consistently forms smaller counterface scars than the BN2.5 composite, indicating reduced contact area and lower COF. Overall, h-BN content critically affects the material transfer: optimal addition improves softening resistance and minimizes transfer, whereas excessive h-BN increases brittleness, promotes cracking, and undermines wear performance.

The lubrication mechanisms of solid lubricants are closely related to surface chemical reactions at different temperatures. Under elevated temperatures, worn surfaces may undergo complex chemical changes that significantly alter tribological performance. To deeply investigate the lubrication mechanisms of ceramic-reinforced RHEA composites across a wide temperature range, detailed XPS analysis was conducted on worn surfaces of BN2.5 and BN5 composites, as shown in Fig.11 and Fig.12, respectively.

Comparative analysis of high-resolution XPS spectra shows no significant differences in elemental valence states on the worn surfaces across temperatures for BN2.5 and BN5 composites. At RT, N 1s peaks at 398 eV confirm the presence of metal nitrides. Deconvoluted Ta 4f peaks at 22.6 and 24.0 eV correspond to TaN, while Ti 2p peaks at 454 and 460 eV indicate the TiN formation. Additionally, B 1s peaks at 192 eV in both composites confirm the presence of metal borides at RT, 300, and 600 ℃. Notably, deconvoluted metal nitride peaks disappear above 300 ℃, indicating oxidation, decomposition, or spalling during the high-temperature friction. In contrast, boride-related peaks remain detectable at 600 °C. Ti spectra peaks exist at 454.9, 456.6, 458.9, and 464.2 eV, confirming the presence of Ti_2O_3 and TiO_2 at RT, and TiO_2 is the dominant phase at elevated temperatures due to enhanced oxidation. Cr peaks at 573.4 ($2p_{3/2}$) and 583.2 ($2p_{1/2}$) eV are also observed at RT. High-resolution XPS spectra from 300 °C to 1000 ℃ consistently reveal the existence of metallic Ta/Mo and their oxides (Ta_2O_5, MoO_3, TiO_2, and Cr_2O_3), indicating minimal compositional changes with temperature. This result suggests that element composition is not the primary factor influencing the wear resistance or wear mechanism transitions. However, increasing the oxide-to-metal peak area ratios with temperature leads to the progressive surface oxidation, which is characterized by diminished metallic signals and intensified oxide signals.

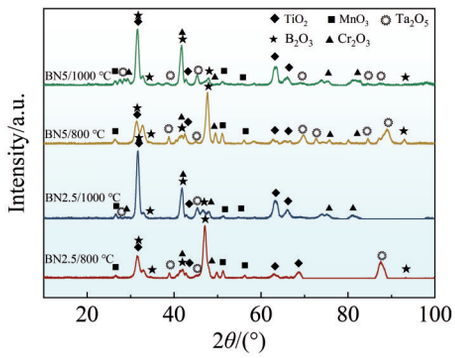

Fig 13 XRD patterns of worn surfaces of BN2.5 and BN5 ceramic-reinforced RHEA composites at different temperatures

Notably, XPS analysis further reveals the presence of B_2O_3 on worn surfaces. XRD patterns of the worn surfaces of BN2.5 and BN5 composites at different temperatures are shown in Fig.13, which further confirms the presence of B_2O_3 on the worn surface. As an oxide with high ionic potential, B_2O_3 effectively screens metal cations and reduces their interactions with other cations, thereby decreasing shear strength at sliding interfaces and smoothing the friction process[62–63]. Additionally, the low melting point of B_2O_3 enables its rheological behavior at elevated temperatures, which suppresses the volatilization of MnO_3 from worn surfaces and promotes the formation of denser and more complete oxide tribolayers in the composites. Consequently, the formation of B_2O_3 on worn surfaces significantly contributes to the decrease in COFs of both BN2.5 and BN5 composites.

4 Conclusions

1) The addition of h-BN promotes in-situ formation of uniformly dispersed hard ceramic phases, including (Ti, Ta)N, TaB_2, and MoB, within the bcc matrix. Increasing h-BN content results in higher volume fraction of the ceramic phase and improved microhardness.

2) Hard ceramic reinforcements enhance surface strength, suppress adhesive wear, and significantly improve the wear resistance, particularly at RT and intermediate temperatures. $TaMoTiCr(BN)_{2.5}$ composite exhibits an ultralow wear rate of $(1.64\pm0.02)\times10^{-7}$ $mm^3\cdot N^{-1}\cdot m^{-1}$ at RT, while $TaMoTiCr(BN)_5$ composite achieves $(2.39\pm0.11)\times10^{-6}$ $mm^3\cdot N^{-1}\cdot m^{-1}$ at 300 °C.

3) At elevated temperatures, tribolayers composed of dense metallic oxides (Cr_2O_3, Ta_2O_5, MoO_3, and TiO_2) form on the worn surface, isolating the alloy from the Al_2O_3 counterface and enhancing the high-temperature wear resistance. At 1000 °C, $TaMoTiCr(BN)_{2.5}$ composite reaches a wear rate of $(5.22\pm0.17)\times10^{-7}$ $mm^3\cdot N^{-1}\cdot m^{-1}$. Additionally, the presence of lubricious B_2O_3 reduces the interfacial shear strength and contributes to a lower COF.

References

1 Zeng G, Liang Z W, Zhao C J *et al*. *Tribology International*[J], 2025, 204: 110491

2 Wang H P, Liao H, Hu L *et al*. *Advanced Materials*[J], 2024, 36: 2313162

3 Wang H P, Hu L, Xie W J *et al*. *Angewandte Chemie International*[J], 2024, 63: e202400312

4 Li M X, Wang H P, Lin M J *et al*. *Acta Materialia*[J], 2022, 237: 118157

5 Li C, Luo J, Li C J *et al*. *Journal of Materials Science & Technology*[J], 2025, 238: 250

6 Yuan L, Yang Y Z, Gan J *et al*. *Acta Materialia*[J], 2025, 295: 121186

7 Yang Y, Zhao Y L, Li W P *et al*. *Science*[J], 2020, 369(6502): 427

8 Du Y, Hua D P, Zhou Q *et al*. *Composites Part B*[J], 2024, 272: 111222

9 Yuan L, Jiang F Y, Hao D *et al*. *Journal of Materials Science & Technology*[J], 2025, 222: 152

10 He Q F, Wang J W, Chen H A *et al*. *Nature*[J], 2022, 602: 251

11 Wang H, Yang P Y, Zhao W J *et al*. *Nature Communications*[J], 2024, 15: 6782

12 Ge Y X, Guo Y S, Su H *et al*. *Journal of Alloys and Compounds* [J], 2025, 1035: 181289

13 Bhardwaj V, Zhou Q, Zhang F *et al*. *Tribology International*[J], 2021, 160: 107031

14 Wu S Y, Qiao D X, Zhang H T *et al*. *Journal of Materials Science & Technology*[J], 2022, 97: 229

15 Wang B J, Wang Q Q, Lu N *et al*. *Journal of Materials Science & Technology*[J], 2022, 123: 191

16 Dai M, Cao P P, Huang H L *et al*. *Journal of Materials Science & Technology*[J], 2022, 122: 243

17 Zhang E K, Tang Y, Wen M W *et al*. *International Journal of Refractory Metals and Hard Materials*[J], 2022, 103: 105780

18 Yao J Q, Liu X W, Gao N *et al*. *Intermetallics*[J], 2018, 98: 79

19 Pei X H, Du Y, Wang H M *et al*. *Corrosion Science*[J], 2023, 224: 111527

20 Schellert S, Gorr B, Laube S *et al*. *Corrosion Science*[J], 2021, 192: 109861

21 Li T, Hu M C, Pei X H *et al*. *Tribology International*[J], 2024, 198: 109850

22 Zhang Z Q, Yao X Y, Pei X H *et al*. *Surface and Coatings Technology*[J], 2025, 515: 132657

23 Pei X H, Du Y, Wang H M *et al*. *Wear*[J], 2024, 558–559: 205572

24 Song Q T, Xu J. *Corrosion Science*[J], 2020, 167: 108513

25 Thirathipviwat P, Onuki Y, Vishnu J *et al*. *Materials Letters*[J], 2023, 339: 134105

26 Pole M, Sadeghilaridjani M, Shittu J *et al*. *Journal of Alloys and Compounds*[J], 2020, 843: 156004

27 Guo Z H, Shen X Y, Liu F *et al*. *Journal of Alloys and Compounds*[J], 2023, 960: 170739

28 Shen X Y, Guo Z H, Liu F. *Journal of Alloys and Compounds*[J], 2024, 990: 174459

29 Gu Y L, Yi M L, Chen Y *et al*. *Materials Characterization*[J], 2022, 193: 112300

30 Deng L, Bai C Y, Jiang Z T *et al*. *Materials Science and Engineering A*[J], 2021, 822: 141642

31 Liu X L, Zhu K, Zhong L M *et al*. *Journal of Materials Science* [J], 2024, 59: 18196

32 Qian W F, Ning B K, Wang S *et al*. *Advanced Functional Materials*[J], 2024, 35: 2418312

33 Hou J H, Qian B N, Zhu Z G *et al*. *Composites Part B: Engineering*[J], 2024, 278: 111428.

34 Pei X H, Du Y, Li T *et al*. *Materials Characterition*[J], 2023, 201: 112956

35 Sheikh S, Bijaksana M K, Motallebzadeh A *et al*. *Intermetallics* [J], 2018, 97: 58

36 Müller F, Gorr B, Christ H J *et al*. *Corrosion Science*[J], 2019, 159: 108161

37 Schellert S, Weber M, Christ H J *et al*. *Corrosion Science*[J], 2023, 211: 110885

38 Hu M C, Li T, Du Y *et al*. *Tribology International*[J], 2024, 199: 110043

39 Wu Y H, Yang H J, Guo R P *et al*. *Wear*[J], 2020, 460–461: 203452

40 Ma X D, Unertl W N, Erdemir A. *Journal of Materials Research* [J], 1999, 14: 3455

41 Xu Z Q, Ma Z L, Tan Y *et al*. *Scripta Materialia*[J], 2022, 206: 114230

42 Maity A, Grenadier S J, Li J *et al*. *Appliex Physics Letter*[J], 2020, 116: 142102

43 Roy S, Zhang X, Puthirath A B *et al*. *Advanced Materials*[J], 2021, 33: 2101589

44 Tabrizi A T, Aghajani H, Saghafian H *et al*. *Tribology International*[J], 2021, 155: 106772

45 Ma K, Feng L, Zhao Y C *et al*. *Rare Metal Materials and Engineering*[J], 2024, 53(12): 2747

46 Jin J, Wang W, Chen X C. *Materials*[J], 2019, 12(1): 427

47 Wyatt B C, Yang Y, Michalowski P P *et al*. *Science*[J], 2025, 389(6764): 1054

48 Liu C, Dong F Y, Zhang Y *et al*. *Intermetallics*[J], 2025, 287: 109019

49 Moniri S, Yang Y, Ding J *et al*. *Nature*[J], 2023, 624: 564

50 Liu C, Gu X L, Zhang K *et al*. *Physical Review B*[J], 2022, 105: 024105

51 Zuo Y, Liu Z B, Zhao W *et al*. *International Journal of Refractory Metals and Hard Materials*[J], 2023, 110: 105997

52 Huang Y, Chen Z, Wagner A *et al*. *Acta Materialia*[J], 2023, 255: 119027

53 Wang X H, Liu S W, Zhao G L *et al*. *Journal of Tribology*[J], 2022, 144: 031402

54 Du Y, Zhou Q, Li S *et al*. *Advanced Functional Materials*[J], 2025: e07634
55 Wang Haiming, Du Yin, Pei Xiafeng *et al*. *Acta Metallurgica Sinica*[J], 2024, 60(7): 937 (in Chinese)
56 Du Y, Li T, Zhou Q *et al*. *Carbon*[J], 2024, 229: 119503
57 Chen M, Lan L W, Shi X H *et al*. *Journal of Alloys and Compounds*[J], 2019, 777: 180
58 Fan X, Zheng S J, Ren S M *et al*. *Materials Characterization*[J], 2022, 191: 112
59 Zhang Q, Ge J R, Zhang B B *et al*. *Ceramics International*[J], 2022, 48: 3109
60 Vo T D, Tran B, Tieu A K *et al*. *Tribology International*[J], 2021, 160: 107017
61 Hao Q, Lyu G J, Pineda E *et al*. *International Journal of Plasticity*[J], 2022, 154: 103288
62 Vo T D, Tran B, Tieu A K *et al*. *Tribology International*[J], 2022, 172: 107588
63 Kasar A K, Subin J A, Brian D S *et al*. *Journal of Materials Engineering and Performance*[J], 2025, 34: 11649

原位陶瓷增强TaMoTiCr难熔高熵合金复合材料的宽温域摩擦学性能

高晨光，裴旭辉，陈　灼，王瀚铭，胡明川，杜　银，王海丰
(西北工业大学 凝固技术全国重点实验室 先进润滑与密封材料研究中心，陕西 西安 710072)

摘　要：通过放电等离子烧结技术制备了原位陶瓷相增强的TaMoTiCr难熔高熵合金复合材料，并分别添加2.5wt%和5.0wt%的h-BN。结果表明：h-BN的添加促进了(Ti, Ta)N、TaB_2和MoB陶瓷相在体心立方基体中的均匀形成，使显微硬度显著提升至1136.95 HV。摩擦学测试结果表明：添加2.5wt% h-BN的复合材料在室温下表现卓越，磨损率低至1.64×10^{-7} $mm^3\cdot N^{-1}\cdot m^{-1}$；而添加5.0wt% h-BN的复合材料在300 ℃时性能最优。在800 ℃以上高温条件下，材料表面形成了富含Cr_2O_3、TiO_2和B_2O_3的润滑氧化摩擦层，有效降低了摩擦与磨损。添加2.5wt% h-BN的复合材料在1000 ℃时磨损率仅为5.22×10^{-7} $mm^3\cdot N^{-1}\cdot m^{-1}$。该原位陶瓷增强策略显著提升了难熔高熵合金在宽温域内的耐磨性能，为先进航空航天应用提供了重要技术路径。

关键词：难熔高熵合金陶瓷复合材料；原位陶瓷相；摩擦学性能；放电等离子烧结

作者简介：高晨光，男，2002年生，硕士生，西北工业大学凝固技术全国重点实验室先进润滑与密封材料研究中心，陕西 西安 710072，E-mail：2021301206@mail.nwpu.edu.cn